Large Polarization and Susceptibilities in Artificial Morphotropic Phase Boundary $PbZr_{1-x}Ti_xO_3$ Superlattices

*Eduardo Lupi, Anirban Ghosh, Sahar Saremi, Shang-Lin Hsu, Shishir Pandya, Gabriel Velarde, Abel Fernandez, Ramamoorthy Ramesh, Lane W. Martin**

E. Lupi, Dr. A. Ghosh, S. Saremi, Dr. S. Pandya, G. Velarde, Abel Fernandez, Prof. R. Ramesh, Prof. L. W. Martin
Department of Materials Science and Engineering
University of California, Berkeley
Berkeley, California 94720, USA
Email: lwmartin@berkeley.edu

S.L. Hsu, S. Saremi, Prof. R. Ramesh, Prof. L. W. Martin
Materials Sciences Division
Lawrence Berkeley National Laboratory
Berkeley, California 94720, USA

Keywords: ferroelectricity, superlattice, $PbZr_{1-x}Ti_xO_3$, polarization switching, dielectric

The ability to produce atomically-precise, artificial oxide heterostructures provides for the possibility of producing exotic phases and enhanced susceptibilities not found in parent materials. Typical ferroelectric materials either exhibit large saturation polarization away from a phase boundary or large dielectric susceptibility near a phase boundary. Here, we attain both large ferroelectric polarization and dielectric permittivity wherein fully-epitaxial $(PbZr_{0.8}Ti_{0.2}O_3)_n/(PbZr_{0.4}Ti_{0.6}O_3)_{2n}$ (n = 2, 4, 6, 8, 16 unit cells) superlattices are produced such that the overall film chemistry is at the morphotropic phase boundary, but constitutive layers are not. Long- (n ≥ 6) and short-period (n = 2) superlattices reveal large ferroelectric saturation polarization (P_s = 64 μC cm^{-2}) and small dielectric permittivity ($\varepsilon_r \approx 400$ at 10 kHz). Intermediate-period (n = 4) superlattices, however, exhibit both large ferroelectric saturation polarization (P_s = 64 μC cm^{-2}) and dielectric permittivity (ε_r = 776 at 10 kHz). First-order reversal curve analysis reveals the presence of switching distributions for each

This is the author manuscript accepted for publication and has undergone full peer review but has not been through the copyediting, typesetting, pagination and proofreading process, which may lead to differences between this version and the Version of Record. Please cite this article as doi: 10.1002/aelm.201901395.

parent layer and a third, interfacial layer wherein superlattice periodicity modulates the volume fraction of each switching distribution and thus the overall material response. This reveals that deterministic creation of artificial superlattices is an effective pathway for designing materials with enhanced responses to applied bias.

Superlattices comprised of thin layers of ferroelectric and/or dielectric materials provide ample opportunity for designing artificial heterostructures with tunable and emergent properties. For example, ferroelectrics can exhibit large susceptibilities to electric fields, stress, temperature, *etc*. which can be enhanced by the competition of structure and polarization between phases and can even lead to the development of novel order parameters.[1–3] In this regard, ferroelectric-dielectric superlattices have been widely studied[4,5] with particular interest on $BaTiO_3/SrTiO_3$[6–12] and $PbTiO_3/SrTiO_3$ superlattices.[13–15] In $PbTiO_3/SrTiO_3$ superlattices alone, for example, researchers have observed the evolution of novel order (*i.e.*, improper ferroelectricity),[14] emergent, smoothly-evolving polar structures (*e.g.*, vortices and skyrmions),[16,17] and even classical flux-closure-domain structures depending on the periodicity and strain state.[13] Considerably less work, however, has focused on superlattices of two different ferroelectric materials[18,19] wherein differences in symmetry,[20] polarization magnitude and direction, transition temperature,[21] *etc*. provide for an alternative approach to novel and/or enhanced responses and phases. In this regard, the $PbZr_{1-x}Ti_xO_3$ system provides interesting opportunities as there are both zirconium-rich rhombohedral and titanium-rich tetragonal phases that are bridged by a morphotropic phase boundary[22,23] wherein those phases compete and provide for interesting properties (**Figure 1**a). Polarization rotation at this phase boundary enables an easier route to

switching at much lower coercive fields and thus enhances susceptibilities. While there has been considerable research on the compositional evolution of structure and properties in this system,[24–26] little work exists on the creation of artificial heterostructures and superlattices.[27–29] That which does exist focuses on long-period (*i.e.*, layers of thickness ≥ 30 nm), ferroelectric-ferroelectric heterostructures. We propose the exploration of short-period (down to 2 unit cells) ferroelectric-ferroelectric superlattices bridged across the morphotropic phase boundary in the $PbZr_{1-x}Ti_xO_3$ system as a potential route to enhanced functionalities. Such a systematic study of ultra-thin superlattice periodicities can elucidate the complex interplay of competing energy terms (*e.g.*, elastic, electrostatic, gradient, *etc*.) present in ferroelectric systems.

Large susceptibilities in the $PbZr_{1-x}Ti_xO_3$ system have historically been attained by selecting materials in the compositional vicinity of the morphotropic phase boundary.[30–32] This typically comes as a trade-off with saturation polarization, as polarization diminishes and susceptibility rises at the phase transition. Here, we take advantage of unit-cell-precise growth to introduce ferroelectric-ferroelectric interfaces as an additional design parameter wherein the material response can be tuned by both composition and superlattice periodicity. We likewise focus on heterostructures with overall chemistry near the morphotropic phase boundary, but built from compositions far from the phase boundary itself: rhombohedral $PbZr_{0.8}Ti_{0.2}O_3$ and tetragonal $PbZr_{0.4}Ti_{0.6}O_3$. Using reflection high-energy electron diffraction (RHEED)-assisted pulsed-laser deposition, we create atomically-precise $(PbZr_{0.8}Ti_{0.2}O_3)_n/(PbZr_{0.4}Ti_{0.6}O_3)_{2n}$ (n = 2, 4, 6, 8, and 16 unit cells) superlattices with overall film chemistry of $PbZr_{0.53}Ti_{0.47}O_3$. As compared to uniform films of the parent materials, the superlattice structures exhibit both large saturation polarization (P_s = 64 μC cm^{-2}) and

dielectric susceptibility (ε_r = 776 at 10 kHz for n = 4 superlattices). ac field-dependent dielectric measurements suggest the presence of both phase-boundary- and parent-like switching events. First-order reversal curve studies reveal separate switching events for each of the parent layers in addition to a third interfacial layer. Ultimately, this reveals that artificial superlattices can be deterministically designed as an effective pathway for enhanced responses to external biases.

Rhombohedral $PbZr_{0.8}Ti_{0.2}O_3$ and tetragonal $PbZr_{0.4}Ti_{0.6}O_3$ were chosen for this work because they are robust ferroelectric phases that differ in terms of symmetry, polarization direction, and have relatively close lattice parameters (a = 4.115 Å for $PbZr_{0.8}Ti_{0.2}O_3$ and a = 4.008 Å, c = 4.134 Å for $PbZr_{0.4}Ti_{0.6}O_3$) such that high-quality superlattices of various periods can be synthesized. All heterostructures are grown on 20 nm $Ba_{0.5}Sr_{0.5}RuO_3/PrScO_3$ (110) substrates (which were chosen because of the compressive strain[33] that is imposed on both the $PbZr_{0.8}Ti_{0.2}O_3$ (-2.5%) and $PbZr_{0.4}Ti_{0.6}O_3$ (-0.3%) layers). Details of the growth are provided (Experimental Section). To begin, it has been observed in prior studies that the exact chemical composition of the morphotropic phase boundary in $PbZr_{1-x}Ti_xO_3$ can shift (slightly) towards higher concentrations of zirconium with compressive epitaxial strain.[34] Thus, a preliminary study was conducted to assess the average superlattice composition required to access phase-boundary-like behavior, namely an enhancement of dielectric susceptibility.[35] To sweep across various average compositions, 80-nm-thick $(PbZr_{0.8}Ti_{0.2}O_3)_n/(PbZr_{0.4}Ti_{0.6}O_3)_m$ superlattices with varying $n \times m$ ratios were produced while the total periodicity $n + m$ was held constant at 12 unit cells (specifically we studied $n \times m$ = 7 × 5, 5 × 7, 4 × 8, and 3 × 9, corresponding to average superlattice compositions of $PbZr_{0.63}Ti_{0.37}O_3$, $PbZr_{0.57}Ti_{0.43}O_3$, $PbZr_{0.53}Ti_{0.47}O_3$, and $PbZr_{0.5}Ti_{0.5}O_3$, respectively).

Subsequent θ-2θ X-ray diffraction studies reveal high-quality, epitaxial superlattices (Figure S1a, Supporting Information). Capacitor-based dielectric-permittivity measurements (Experimental Section), indicate an enhancement of the out-of-plane dielectric response, akin to that expected near the phase boundary, for the 4 × 8 superlattices (Figure S1b, Supporting Information) which corresponds to an average composition of $PbZr_{0.53}Ti_{0.47}O_3$. Based on this observation, for the remainder of the study we fixed the overall heterostructure chemistry to be $PbZr_{0.53}Ti_{0.47}O_3$ thus requiring the production of various $n \times 2n$ superlattices.

At this overall film composition, periodicity-dependent studies were completed. Here, we focus on 80-nm-thick heterostructures including the following variants: 1) superlattice structures of the form $(PbZr_{0.8}Ti_{0.2}O_3)_n/(PbZr_{0.4}Ti_{0.6}O_3)_{2n}$ (with n = 2, 4, 6, 8, and 16), 2) bilayer structures with 27 nm of $PbZr_{0.8}Ti_{0.2}O_3$ and 53 nm of $PbZr_{0.4}Ti_{0.6}O_3$ (*i.e.*, a 1:2 ratio of the parent materials, equivalent to the ratio found in all the superlattices), 3) parent rhombohedral $PbZr_{0.8}Ti_{0.2}O_3$, 4) parent tetragonal $PbZr_{0.4}Ti_{0.6}O_3$, and 5) morphotropic phase boundary $PbZr_{0.52}Ti_{0.48}O_3$. The production of high-quality superlattices was enabled by our ability to achieve layer-by-layer growth as monitored during deposition via RHEED (Figure 1b,c). Throughout (and after growth) the presence of a "streaky" RHEED pattern demonstrates a persistent 2D-growth mode and a smooth surface for a representative superlattice growth (inset, Figure 1b). θ-2θ X-ray diffraction studies of the resulting superlattices reveal epitaxial, 00*l*-oriented films with superlattice peaks varying as a function of superlattice periodicity (Figure 1c). Wide-angle θ-2θ X-ray studies show no secondary phases and high-quality, epitaxial growth for all heterostructure variants (Figure S2, Supporting Information). Reciprocal space maps about the 103_{pc}-diffraction conditions for all superlattice heterostructures show fully-strained films (Figure S3, Supporting Information).

Z-contrast, high-angle annular dark-field (HAADF) scanning transmission electron microscopy (STEM) imaging and energy dispersive spectroscopy (EDS) studies were completed for two superlattice structures [$(PbZr_{0.8}Ti_{0.2}O_3)_n/(PbZr_{0.4}Ti_{0.6}O_3)_{2n}$ with n = 6, 8] and reveal the production of high-quality heterostructures with smooth interfaces that exhibit no obvious defect structures (Figure S4, Supporting Information). Due to the similar chemistry between the layers (*i.e.*, both layers in the superlattice contain lead, zirconium, and titanium) the z-contrast between the layers is not as distinct as one might expect for a superlattice made from vastly different materials. To confirm the production of the superlattice structures, EDS studies were employed to map the local chemical variations throughout the superlattice structure (Figure 1d). The EDS signatures from the titanium and zirconium are observed to oscillate or alternate in intensity due to the chemical variations in each layer of the superlattice (*i.e.*, from zirconium-rich $PbZr_{0.8}Ti_{0.2}O_3$ to titanium-rich $PbZr_{0.4}Ti_{0.6}O_3$) and this helps identify the superlattice structure in the absence of robust z-contrast. All told, the STEM and EDS data, in conjunction with extensive RHEED and X-ray diffraction studies, confirm that high-quality superlattices of various periodicities can be produced. Thus, it is appropriate to proceed to study the impact of superlattice design on dielectric and ferroelectric response.

Frequency-dependent dielectric-permittivity measurements demonstrate low-loss response in all heterostructure variants, but a strong superlattice periodicity dependence of the permittivity itself (**Figure 2**a-b). Similar studies were completed for the parent tetragonal $PbZr_{0.4}Ti_{0.6}O_3$ (ε_r = 362 at 10 kHz), the parent rhombohedral $PbZr_{0.8}Ti_{0.2}O_3$ (ε_r = 492 at 10 kHz), and morphotropic phase boundary $PbZr_{0.52}Ti_{0.48}O_3$ (ε_r = 799 at 10 kHz) (Figure 2a). Both the $PbZr_{0.4}Ti_{0.6}O_3$ and $PbZr_{0.8}Ti_{0.2}O_3$ show low dielectric loss, while the $PbZr_{0.52}Ti_{0.48}O_3$

shows slightly increased loss consistent with the complex structural evolution under applied external fields (Figure 2b). This range of properties provides an important framework in which to probe the superlattice heterostructures. The dielectric permittivity hovers around ≈400 (at 10 kHz) for the bilayer heterostructures and all long-period superlattices ($n \geq 6$). At the other end of the spectrum, short-period superlattices ($n = 2$) also exhibit permittivity in a similar range. Intermediate-period superlattices ($n = 4$), however, display dramatically enhanced permittivity (≈776 at 10 kHz, Figure 2c). Naively, one might expect that reducing the superlattice period should result in a more uniform, morphotropic-phase-boundary-like heterostructure and, thus, systematically increasing dielectric response. Our observations, however, suggest a more complex evolution of dielectric response with superlattice periodicity and begs the question: what gives rise to the dielectric enhancement in the $n = 4$ superlattices?

One potential explanation is that reducing the size (or thickness) of the ferroelectric layers is destabilizing the polarization and effectively lowering the Curie temperature which would result in an enhanced room-temperature dielectric permittivity in the ultra-thin superlattices. To probe this concept, temperature-dependent dielectric measurements were completed on the parent $PbZr_{0.4}Ti_{0.6}O_3$ and $PbZr_{0.8}Ti_{0.2}O_3$ heterostructures and the $n = 4$ superlattices (Figure S5, Supporting Information). These studies reveal, however, that enhancement in dielectric response does not stem simply from a lower transition temperature as Curie-Weiss analysis of the phase transition shows that the transition temperatures are 580, 500, and 560°C for $PbZr_{0.4}Ti_{0.6}O_3$, $PbZr_{0.8}Ti_{0.2}O_3$, and $n = 4$ superlattice heterostructures, respectively. To further explore the phase-boundary behavior of this specific superlattice periodicity and deconvolute contributions to the dielectric response, Rayleigh dielectric

measurements were employed (Experimental Section). Rayleigh studies utilize an ac-field-dependent measurement to probe the behavior of ferroelectric materials in three different regimes: low, high, and switching fields. Both the low- and high-field regimes are sub-switching linear regimes from which the reversible and irreversible extrinsic contributions to dielectric response, respectively, can be extracted. In the low-field regime,[36] an enhanced field-independent constant permittivity represented by the reversible Rayleigh parameter ε'_{ini} indicates large intrinsic lattice and reversible extrinsic contributions.[37] In the high-field (Rayleigh regime), a steep linear slope indicated by the Rayleigh coefficient α' is typical of an enhanced irreversible contribution.[38] Thus the overall dielectric response is represented as:

$$\varepsilon_r = \varepsilon'_{ini} + \alpha' E_0. \quad (1)$$

Analysis of the Rayleigh studies at sub-switching fields reveals both parent phases and the bilayer heterostructures to have small ε'_{ini} ($\lesssim 360$) and α' ($\lesssim$ 4 cm kV^{-1}) (Figure S6, Supporting Information), while the phase-boundary $PbZr_{0.52}Ti_{0.48}O_3$ exhibits large ε'_{ini} (865) and α' (87.6 cm kV^{-1}) (Table 1). In this context, the intermediate-period superlattices (n = 4) demonstrate enhanced ε'_{ini} (805) and α' (32 cm kV^{-1}) (Figure 2d); values considerably larger than those in all other superlattices and similar to literature values for bulk $PbZr_{0.52}Ti_{0.48}O_3$.[37] This suggests that this periodicity (n = 4) behaves quite similarly to a phase-boundary material, yet it was created from compositions away from the phase boundary. Motivated by the observation of this strong periodicity dependence of the small-field dielectric response, we proceed to study ferroelectric behavior under large applied fields wherein we expect to observe hysteresis phase-boundary-like switching behavior.

Polarization and current-electric field hysteresis loops (for brevity shown only at 10 kHz) demonstrate the evolution of both the polarization and switching current in the heterostructures. Hysteresis loops for the parent phases $PbZr_{0.8}Ti_{0.2}O_3$ (**Figure 3**a) and $PbZr_{0.4}Ti_{0.6}O_3$ (Figure 3b) show a large saturation polarization P_s = 67 μC cm^{-2} and a single switching event as illustrated by the single current peak (yellow for $PbZr_{0.8}Ti_{0.2}O_3$ and blue for $PbZr_{0.4}Ti_{0.6}O_3$). The $PbZr_{0.52}Ti_{0.48}O_3$ phase exhibits a much smaller saturation polarization (P_s = 45 μC cm^{-2}, Figure 3c). The bilayer (Figure 3d) and superlattice heterostructures (Figure 3e-i) exhibit a consistent P_s = 64 μC cm^{-2}. In the current loops, two switching events are evident (as illustrated by the two current peaks) with an intensity ratio that is related to the volume fraction of the parent phases in the heterostructures. The two switching events, therefore, are hypothesized to be related to the two parent phases present. The puzzling conclusion from this data is that the intermediate-period superlattices (n = 4) do not behave like the phase-boundary film, but instead are similar to the other superlattice periodicities which show indications of mixed-parent-phase behavior.

While the large-field switching response is consistent among the various superlattices, the small-field dielectric response (Figure 2) varies greatly with periodicity. Intermediate-period superlattices (n = 4) have the most interesting behavior, wherein there is both enhanced permittivity (*i.e.*, large ε_r = 776 at 10 kHz, ε'_{ini} = 805 and α' = 32 cm kV^{-1}) akin to phase-boundary-like response and simultaneously large saturation polarization (P_s = 64 μC cm^{-2}) akin to the parent-phase materials and other superlattices. This unusual combination of large dielectric permittivity and ferroelectric polarization in the intermediate-period superlattices (n = 4) calls for further study as a function of external bias. Here, we extend the dielectric Rayleigh measurements (which are typically performed in sub-switching fields) to

the third regime – the switching-field regime – at higher fields. Parent phases $PbZr_{0.8}Ti_{0.2}O_3$ and $PbZr_{0.4}Ti_{0.6}O_3$ exhibit peaks in the dielectric response corresponding to switching at relatively large fields (80-125 kV cm^{-1}), whereas phase-boundary $PbZr_{0.52}Ti_{0.48}O_3$ exhibits a peak corresponding to switching at lower fields (25-60 kV cm^{-1}) (**Figure 4**a). This behavior can be used as a reference frame to understand the response of the superlattice heterostructures which exhibit features similar to both $PbZr_{0.52}Ti_{0.48}O_3$ (*i.e.*, low-field response within the switching-field regime) and the parent phases $PbZr_{0.8}Ti_{0.2}O_3$ and $PbZr_{0.4}Ti_{0.6}O_3$ (*i.e.*, high-field response within the switching-field regime). While all bilayer and superlattice heterostructures exhibit some features of parent- and phase-boundary-like character in the switching-field regime, the short- and intermediate-period superlattices (n = 2, 4) have a particularly pronounced phase-boundary character and the long-period superlattices ($n \geq 6$) and bilayer heterostructures have pronounced parent character (Figure 4b). This mixed phase-boundary- and parent-like character suggests that while aspects of the response of the parent $PbZr_{0.8}Ti_{0.2}O_3$ and $PbZr_{0.4}Ti_{0.6}O_3$ materials are maintained, the intimate interfacing of these materials gives rise to a response more akin to $PbZr_{0.52}Ti_{0.48}O_3$, most likely at the interface between the two layers. Additional insight in this regard can be extracted from the dielectric loss data taken simultaneously. Again, the $PbZr_{0.52}Ti_{0.48}O_3$ phase exhibits a peak in loss at lower fields (20-50 kV cm^{-1}) while the parent phases $PbZr_{0.8}Ti_{0.2}O_3$ and $PbZr_{0.4}Ti_{0.6}O_3$ exhibit peaks in loss at relatively larger fields (50-90 kV cm^{-1}) (Figure 4c). Likewise, all superlattice heterostructures exhibit mixed loss character (*i.e.*, loss signatures at both low and high fields), but in general the shorter the superlattice period ($n \leq 4$) the larger the proportion of the small-field effects, whereas the opposite trend is observed for long-period superlattices. In turn, this suggests that the superlattices with more interfaces exhibit

more phase-boundary-like switching behavior, thus a higher permittivity in small fields, while maintaining aspects of ferroelectric polarization switching akin to that of the parent phases $PbZr_{0.8}Ti_{0.2}O_3$ and $PbZr_{0.4}Ti_{0.6}O_3$.

These large-field Rayleigh studies suggest the potential for a complex switching process wherein – particularly in the superlattices – multiple switching phenomena including aspects not only related to the parent phases ($PbZr_{0.8}Ti_{0.2}O_3$ and $PbZr_{0.4}Ti_{0.6}O_3$), but also to the phase boundary $PbZr_{0.52}Ti_{0.48}O_3$. To probe this idea, first-order reversal curve (FORC) analysis, which reveals the Preisach distribution of switchable units (so-called hysterons) over bias and coercive fields,[39] was performed by measuring a series of minor loops at 1 kHz. All heterostructures were first poled with a negative bias and gradually switched with positive biases of increasing magnitude (Experimental Section and Figure S7, Supporting Information).[40] Analyses of the $PbZr_{0.8}Ti_{0.2}O_3$ (**Figure 5**a) and $PbZr_{0.4}Ti_{0.6}O_3$ (Figure 5b) parent phases reveal singular FORC distributions wherein $PbZr_{0.4}Ti_{0.6}O_3$ has a larger coercive field (~70 kV cm^{-1} versus ~50 kV cm^{-1}). The $PbZr_{0.52}Ti_{0.48}O_3$ phase-boundary material (Figure 5c) demonstrates a much lower coercive field (~20 kV cm^{-1}) consistent with the polarization-electric field hysteresis loops (Figure 3). The bilayer heterostructures (Figure 5d) exhibit two distinct distributions likely arising from the two parent-phase layers. These two switching distributions are matched in coercive field (~80 kV cm^{-1}), which suggests that the entirety of the film switches together to prevent large penalties in electrostatic energy. Because two-thirds of the total ferroelectric layer volume is comprised of $PbZr_{0.4}Ti_{0.6}O_3$, which has a large coercive field, it sets the overall coercive field for the entire film and pushes the switching distribution of the $PbZr_{0.8}Ti_{0.2}O_3$ component to match in coercive field. In the superlattice heterostructures (Figure 5e-h), a third distribution emerges at lower

coercive fields (~36 kV cm^{-1}) which can be attributed to a phase-boundary-like interfacial region. To better quantify the periodicity-dependent evolution of the different switching distributions, a line-profile of the FORC distribution was taken at a reversal field of ~70 kV cm^{-1} (cutting through both the distributions attributed to parent $PbZr_{0.4}Ti_{0.6}O_3$ and phase-boundary $PbZr_{0.52}Ti_{0.48}O_3$). As the superlattice periodicity is shortened, two changes are observed. First, there is a decrease in the intensity of the distribution attributed to the parent-$PbZr_{0.4}Ti_{0.6}O_3$-like character simultaneous to an increase in the intensity of the distribution attributed to the phase-boundary-like character (Figure 5i). Second, the distinct switching distributions start to converge as the distribution attributed to the parent-$PbZr_{0.4}Ti_{0.6}O_3$-like character shifts to lower fields.

Additional insight about the evolution of the heterostructures can be extracted by recalling that the Preisach density of each FORC distribution (Figure 5) also indicates a population map of switching fields in a material,[41] thus we can relate the FORC peak intensity to a volume fraction of material responsible for that distribution. For example, in the bilayer heterostructures the ratio of distribution intensities attributed to the parent-$PbZr_{0.4}Ti_{0.6}O_3$- (blue) and parent- $PbZr_{0.8}Ti_{0.2}O_3$-like (yellow) character is consistent with the heterostructure volume fraction (66% $PbZr_{0.4}Ti_{0.6}O_3$ and 33% $PbZr_{0.8}Ti_{0.2}O_3$; a 2:1 ratio) (**Figure 6**a). As the superlattice periodicity is shortened, the intensity of the distribution attributed to the parent-$PbZr_{0.4}Ti_{0.6}O_3$-like character decreases and the intensity of the distribution attributed to the phase-boundary-like character (green) increases. The intensity of the distribution attributed to the parent-$PbZr_{0.8}Ti_{0.2}O_3$-like character remains relatively unchanged with periodicity, which is attributed to the larger difference in chemical proximity to the phase-boundary for this composition than the parent-$PbZr_{0.4}Ti_{0.6}O_3$ phase. This

suggests that as the number of interfaces is increased, the fraction of material in the superlattices exhibiting phase-boundary-like character increases – a trend shown schematically (and quantitatively based on the intensity evolution of the FORC distributions; Figure 6b). In the bilayer heterostructures, the predominant character is that of the parent phases; essentially no phase-boundary-like character is observed. Upon transition, first to the n = 8 and then to the n = 4 superlattices, however, increasingly strong phase-boundary-like character is observed in the FORC corresponding to increasing interfacial volume behavior more like that material. In the short-period superlattices (n = 2), the three FORC distributions merge together, albeit with a higher coercive field than in the reference single-layer phase-boundary $PbZr_{0.52}Ti_{0.48}O_3$, suggesting that even in this ultra-thin structure, some remnant parent character is maintained. This also explains why this film retains the same coercive field as other superlattices.

In conclusion, this work examined the role of superlattice periodicity in the observation of simultaneous large susceptibility and polarization in the $PbZr_{1-x}Ti_xO_3$ system. While atomically-precise $(PbZr_{0.8}Ti_{0.2}O_3)_n/(PbZr_{0.4}Ti_{0.6}O_3)_{2n}$ superlattices with overall film chemistry near the morphotropic phase boundary exhibit uniformly large polarization, there is significant superlattice-periodicity-dependent evolution of the dielectric permittivity and switching behavior. FORC studies reveal separate switching events for each of the parent layers in addition to a phase-boundary-like interfacial layer – with the intensity of the latter increasing as the superlattice period is shortened. This corresponds to the creation of a large volume fraction of phase-boundary-like character at the interfaces in these heterostructures such that one can simultaneously achieve large polarization (enabled by the remnant parent character in those layers) and large permittivity (enabled by the emergent interfacial phase-

boundary-like character layers). Ultimately, this study opens a pathway for artificial heterostructure design to enhance responses to external perturbation.

Experimental Section

Heterostructure Growth: All heterostructures were grown via RHEED-assisted pulsed-laser deposition using a KrF excimer laser (248 nm, LPX-300, Coherent), in an on-axis geometry. Films were grown on 20 nm $Ba_{0.5}Sr_{0.5}RuO_3$/$PrScO_3$ (110) single-crystal substrates (Crystec) from ceramic targets. The bottom $Ba_{0.5}Sr_{0.5}RuO_3$ layer was grown at a heater temperature of 700°C in an oxygen-partial pressure of 100 mTorr with a laser fluence of 2.0 J cm^{-2} and a laser repetition rate of 10 Hz. Parent phases $PbZr_{0.8}Ti_{0.2}O_3$ and/or $PbZr_{0.4}Ti_{0.6}O_3$, were deposited at a heater temperature of 610°C in an oxygen-partial pressure of 100 mTorr with a laser fluence of 1.4 J cm^{-2} and a laser repetition rate of 10 Hz using 10% lead-excess targets. $PbZr_{0.52}Ti_{0.48}O_3$ was deposited under the same conditions as the parent phases, again using a 10% lead-excess target. The top electrode, 40 nm $BaSr_{0.5}Ru_{0.5}O_3$, was deposited *in situ* at 610°C and 100 mTorr immediately after the deposition of ferroelectric layer(s). All heterostructures grown were tri-layers of the form: 20 nm bottom electrode, 80 nm total ferroelectric layer(s), and 40 nm top electrode. After deposition, films were cooled down to room temperature in an oxygen pressure of 760 Torr at a rate of 10 ^{0} C min^{-1}.

Ferroelectric and Dielectric Measurements: All electrical measurements were performed on the above noted capacitor structures with symmetric $Ba_{0.5}Sr_{0.5}RuO_3$ electrodes. Top electrodes were lithographically patterned and ion-milled to define 50 μm diameter circular capacitors. Ferroelectric properties were measured using a Precision Multiferroic

Tester (Radiant Technologies). A triangular voltage profile was employed with a maximum bias of up to ±4 V. Ferroelectric hysteresis loops were obtained using a bipolar triangular profile at frequencies ranging from 0.1-10 kHz. Dielectric measurements were carried out using an E4990A Impedance Analyzer (Agilent Technologies) at an ac excitation voltage of 10 mV. Rayleigh dielectric measurements were carried out at a frequency of 1 kHz, wherein the ac-field strength was ramped from 5 mV up to 50 mV for sub-switching regimes and 5 mV to 1 V for switching regimes.

First-Order Reversal Curve (FORC) Analysis: FORC analysis was performed by measuring a series of ascending minor loops at 1 kHz with a monopolar triangular voltage profile between a negative saturation field and variable reversal field E_r. The distribution of elementary switchable units, according to the Preisach model,[38] is mapped out by taking the mixed second derivative of polarization with respect to the actual field (E) and the reversal field (E_r):

$$\rho(E, E_r) = \frac{\delta^2(P_{FORC}(E,E_r))}{2\delta E \delta E_r} \quad (2)$$

The coordinates of the FORC distribution was converted to coercive-field and bias-field axes:

$$E_C = \frac{E_r - E}{2} \text{ and } E_B = \frac{E_r + E}{2} \quad (3)$$

Supporting Information

Supporting Information is available from the Wiley Online Library or from the author.

Acknowledgements

E.L. acknowledges support from the National Science Foundation under grant DMR-1608938. A.G. acknowledges support from the Gordon and Betty Moore Foundation's EPiQS Initiative, under grant GBMF5307. S.S. acknowledges support from the U.S. Department of Energy, Office of Science, Office of Basic Energy Sciences, under Award Number DE-SC-0012375 for the development of ferroelectric thin films. S.P. acknowledges support from the Army Research Office under Grant W911NF-14-1-0104. G.V. acknowledges support from the National Science Foundation under grant DMR-1708615. A.F. acknowledges support from the National Science Foundation under grant OISE-1545907. L.W.M. acknowledges support from the U.S. Department of Energy, Office of Science, Office of Basic Energy Sciences, Materials Sciences and Engineering Division under Contract No. DE-AC02-05-CH11231 (Materials Project program KC23MP) for the growth and study of advanced functional oxide thin films.

Received: ((will be filled in by the editorial staff))
Revised: ((will be filled in by the editorial staff))
Published online: ((will be filled in by the editorial staff))

References

[1] A. Erbil, Y. Kim, R. A. Gerhardt, *Phys. Rev. Lett.* **1996**, *77*, 1628.

[2] P. Zubko, S. Gariglio, M. Gabay, P. Ghosez, J.-M. Triscone, *Annu. Rev. Condens. Matter Phys.* **2011**, *2*, 141.

[3] H. N. Lee, H. M. Christen, M. F. Chisholm, C. M. Rouleau, D. H. Lownde, *Nature* **2005**, *433*, 395.

[4] O. Nakagawara, T. Shimuta, T. Makino, S. Arai, H. Tabata, T. Kawai, *Appl. Phys.*

Lett. **2000**, *77*, 3257.

[5] H. Tabata, H. Tanaka, T. Kawai, *Appl. Phys. Lett.* **1994**, *65*, 1970.

[6] K. Johnston, X. Huang, J. B. Neaton, K. M. Rabe, *Phys. Rev. B* **2005**, *71*, 100103.

[7] T. Shimuta, O. Nakagawara, T. Makino, S. Arai, H. Tabata, T. Kawai, *J. Appl. Phys.* **2002**, *91*, 2290.

[8] Kendra Kathan-Galipeau, Pingping Wu, Yulan Li, Long-Qing Chen, Arsen Soukiassian, Xiaoxing Xi, G. S. Darrell, D. A. Bonnell, *ACS Nano* **2010**, *5*, 640.

[9] N. Ortega, A. Kumar, O. A. Maslova, Y. I. Yuzyuk, J. F. Scott, R. S. Katiyar, *Phys. Rev. B* **2011**, *83*, 144108.

[10] N. Ortega, A. Kumar, O. Resto, O. A. Maslova, Y. I. Yuzyuk, J. F. Scott, R. S. Katiyar, *J. Appl. Phys.* **2013**, *114*, 104102.

[11] B. Bein, H.-C. Hsing, S. J. Callori, J. Sinsheimer, P. V. Chinta, R. L. Headrick, M. Dawber, *Nat. Commun.* **2015**, *6*, 10136.

[12] P. Wu, X. Ma, Y. Li, C. B. Eom, D. G. Schlom, V. Gopalan, L. Q. Chen, *Appl. Phys. Lett.* **2015**, *107*, 122906.

[13] Y. L. Tang, Y. L. Zhu, X. L. Ma, A. Y. Borisevich, A. N. Morozovska, E. A. Eliseev, W. Y. Wang, Y. J. Wang, Y. B. Xu, Z. D. Zhang, S. J. Pennycook, *Science* **2015**, *348*, 547.

[14] E. Bousquet, M. Dawber, N. Stucki, C. Lichtensteiger, P. Hermet, S. Gariglio, J. M. Triscone, P. Ghosez, *Nature* **2008**, *452*, 732.

[15] J. Y. Jo, P. Chen, R. J. Sichel, S. J. Callori, J. Sinsheimer, E. M. Dufresne, M. Dawber, P. G. Evans, *Phys. Rev. Lett.* **2011**, *107*, 55501.

[16] A. K. Yadav, C. T. Nelson, S. L. Hsu, Z. Hong, J. D. Clarkson, C. M. Schlepuëtz, A.

R. Damodaran, P. Shafer, E. Arenholz, L. R. Dedon, D. Chen, A. Vishwanath, A. M. Minor, L. Q. Chen, J. F. Scott, L. W. Martin, R. Ramesh, *Nature* **2016**, *530*, 198.

[17] S. Das, Y. L. Tang, Z. Hong, M. A. P. Gonçalves, M. R. McCarter, C. Klewe, K. X. Nguyen, F. Gómez-Ortiz, P. Shafer, E. Arenholz, V. A. Stoica, S. L. Hsu, B. Wang, C. Ophus, J. F. Liu, C. T. Nelson, S. Saremi, B. Prasad, A. B. Mei, D. G. Schlom, J. Íñiguez, P. García-Fernández, D. A. Muller, L. Q. Chen, J. Junquera, L. W. Martin, R. Ramesh, *Nature* **2019**, *568*, 368.

[18] G. Liu, Q. Zhang, H. H. Huang, P. Munroe, V. Nagarajan, H. Simons, Z. Hong, L. Q. Chen, *Adv. Mater. Interfaces* **2016**, *3*, 1600444.

[19] F. Xue, J. J. Wang, G. Sheng, E. Huang, Y. Cao, H. H. Huang, P. Munroe, R. Mahjoub, Y. L. Li, V. Nagarajan, L. Q. Chen, *Acta Mater.* **2013**, *61*, 2909.

[20] N. Sai, B. Meyer, D. Vanderbilt, *Phys. Rev. Lett.* **2000**, *84*, 5636.

[21] E. D. Specht, H. Christen, D. P. Norton, L. A. Boatner, *Phys. Rev. Lett.* **1998**, *80*, 4317.

[22] B. Jaffe, R. S. Roth, S. Marzullo, *J. Appl. Phys.* **1954**, *25*, 809.

[23] B. Noheda, D. E. Cox, G. Shirane, J. A. Gonzalo, L. E. Cross, S.-E. Park, *Appl. Phys. Lett.* **1999**, *74*, 2059.

[24] R. V. K. Mangalam, J. Karthik, A. R. Damodaran, J. C. Agar, L. W. Martin, *Adv. Mater.* **2013**, *25*, 1761.

[25] J. C. Agar, A. R. Damodaran, M. B. Okatan, J. Kacher, C. Gammer, R. K. Vasudevan, S. Pandya, L. R. Dedon, R. V. K. Mangalam, G. A. Velarde, S. Jesse, N. Balke, A. M. Minor, S. V. Kalinin, L. W. Martin, *Nat. Mater.* **2016**, *15*, 549.

[26] J. C. Agar, A. R. Damodaran, G. A. Velarde, S. Pandya, R. V. K. Mangalam, L. W.

Martin, *ACS Nano* **2015**, *9*, 7332.

[27] H. H. Huang, Q. Zhang, E. Huang, R. Maran, O. Sakata, Y. Ehara, T. Shiraishi, H. Funakubo, P. Munroe, N. Valanoor, *Adv. Mater. Interfaces* **2015**, *2*, 1500075.

[28] D. Bao, R. Scholz, M. Alexe, D. Hesse, *J. Appl. Phys.* **2007**, *101*, 54118.

[29] I. A. Kornev, L. Bellaiche, *Phys. Rev. Lett.* **2003**, *91*, 116103.

[30] S. Pandya, G. A. Velarde, R. Gao, A. S. Everhardt, J. D. Wilbur, R. Xu, J. T. Maher, J. C. Agar, C. Dames, L. W. Martin, *Adv. Mater.* **2019**, *31*, 1803312.

[31] B. Noheda, D. E. Cox, G. Shirane, R. Guo, B. Jones, L. E. Cross, *Phys. Rev. B* **2000**, *63*, 14103.

[32] E. Cross, *Nature* **2004**, *432*, 24.

[33] P.-E. Janolin, *J. Mater. Sci.* **2009**, *44*, 5025.

[34] S. Hoon Oh, H. W. Jang, *Phys. Rev. B* **2000**, *62*, 14757.

[35] N. A. Pertsev, V. G. Kukhar, H. Kohlstedt, R. Waser, *Phys. Rev. B* **2003**, *67*, 54107.

[36] D. A. Hall, P. J. Stevenson, *Ferroelectrics* **1999**, *228*, 139.

[37] N. Bassiri-Gharb, I. Fujii, E. Hong, S. Trolier-Mckinstry, D. V. Taylor, D. Damjanovic, *J. Electroceram.* **2007**, *19*, 47.

[38] R. Xu, J. Karthik, A. R. Damodaran, L. W. Martin, *Nat. Commun.* **2014**, *5*, 3120.

[39] A. Stancu, D. Ricinschi, L. Mitoseriu, P. Postolache, M. Okuyama, *Appl. Phys. Lett.* **2003**, *83*, 3767.

[40] C. R. Pike, A. P. Roberts, K. L. Verosub, *J. Appl. Phys.* **2013**, *85*, 6660.

[41] Y. Kim, A. Kumar, O. Ovchinnikov, S. Jesse, H. Han, D. Pantel, I. Vrejoiu, W. Lee, D. Hesse, M. Alexe, S. V. Kalinin, *ACS Nano* **2012**, *6*, 491.

Figures and Captions

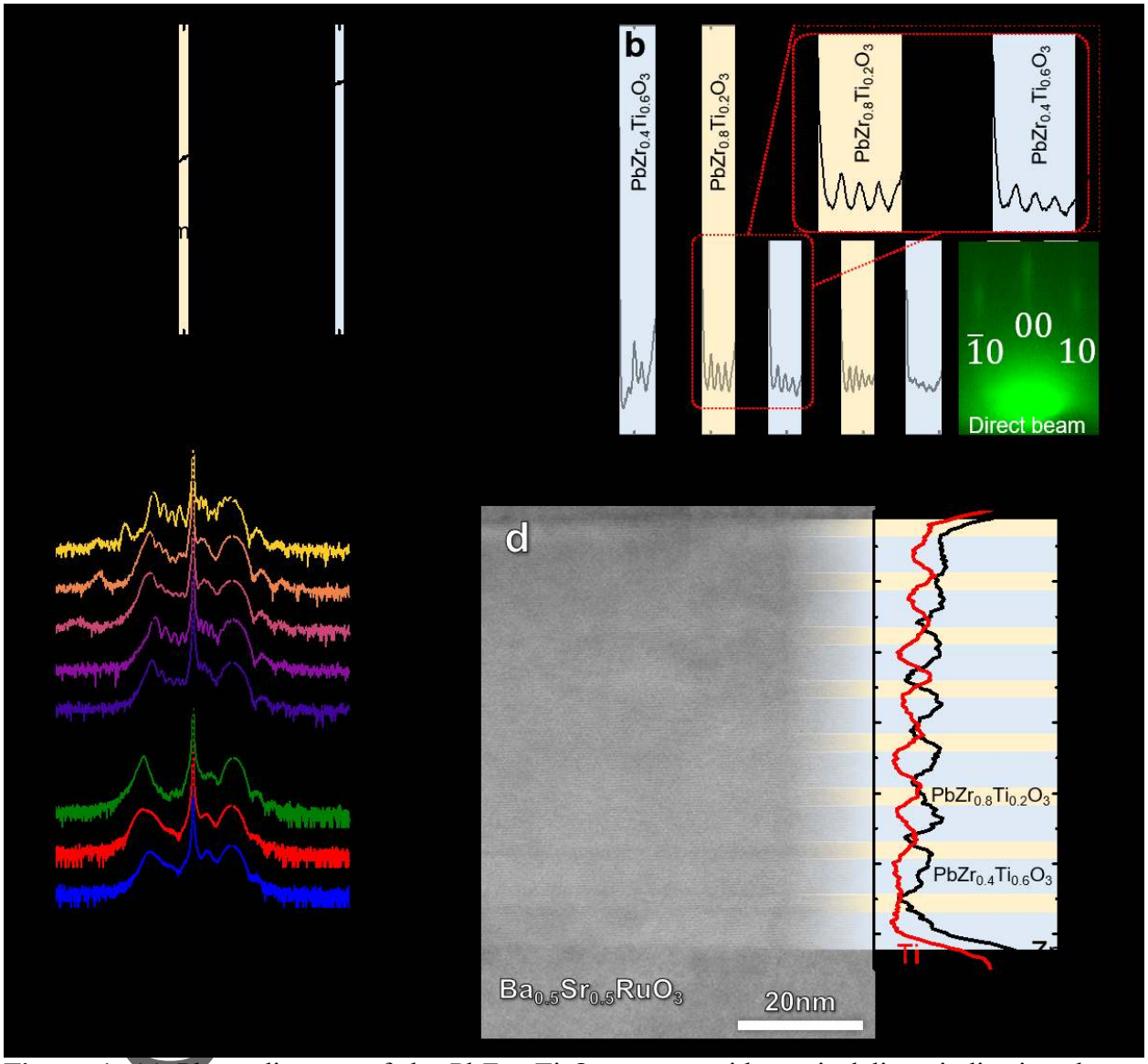

Figure 1. (a) Phase diagram of the $PbZr_{1-x}Ti_xO_3$ system with vertical lines indicating the selected parent compositions. RHEED-assisted pulsed-laser deposition growth of the heterostructures demonstrating (b) persistent layer-by-layer deposition and sharp interface control. (c) θ-2θ X-ray diffraction patterns about the 002-diffraction condition for the various parent, bilayer, and superlattice heterostructures. (d) STEM image with overlaid EDS mapping (right) indicating the production of high-quality superlattice structures.

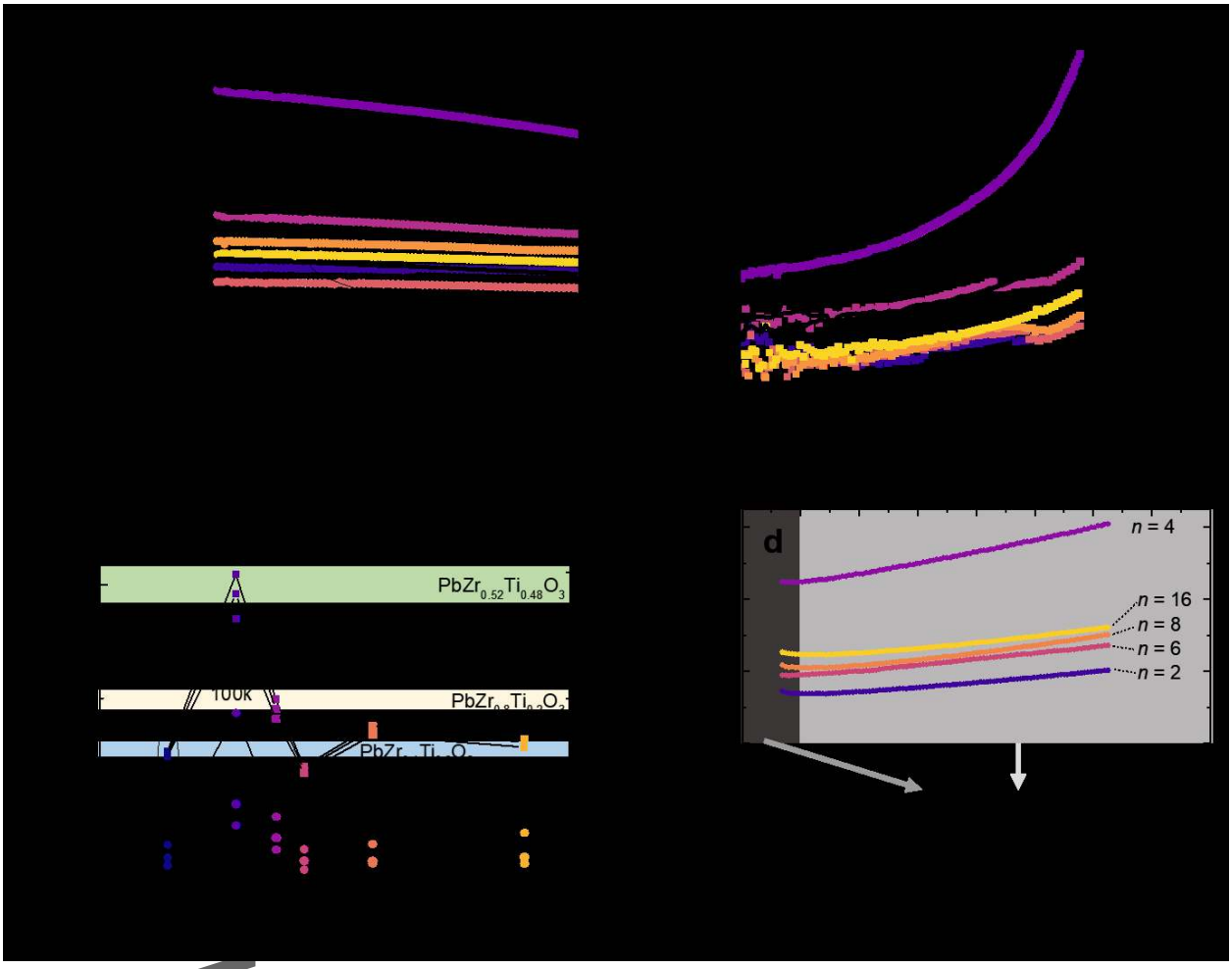

Figure 2. (a) Dielectric permittivity and (b) loss tangent as a function of measurement frequency for the various parent, bilayer, and superlattice heterostructures. (c) Summary of the dielectric response (*i.e.*, permittivity on the left axis and loss on the right axis) as a function of superlattice periodicity demonstrating a strong enhancement at a critical superlattice periodicity of n = 4 unit cells. (d) Rayleigh dielectric measurements at sub-switching fields for the various superlattice heterostructures.

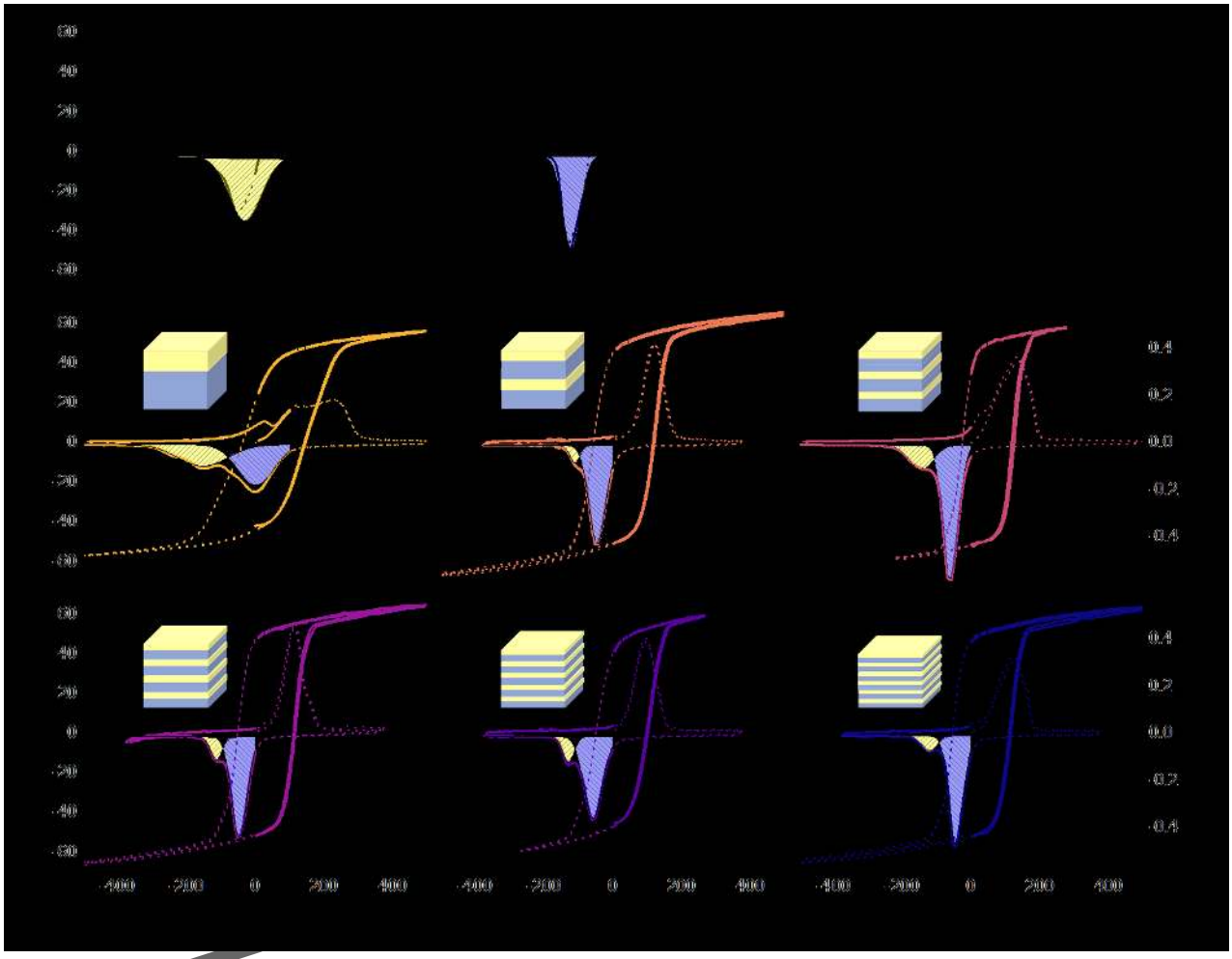

Figure 3. Ferroelectric polarization-electric field hysteresis loops (left axis) and ferroelectric current-electric field loops (right axis) behavior (at 10 kHz) for single-layer parent (a) $PbZr_{0.8}Ti_{0.2}O_3$ and (b) $PbZr_{0.4}Ti_{0.6}O_3$ as well as single-layer (c) phase-boundary $PbZr_{0.52}Ti_{0.48}O_3$ heterostructures together with those of (d) bilayer and superlattice heterostructures with (e) n = 16, (f) n = 8, (g) n = 6, (h) n = 4, and (i) n = 2. Note that the polarization and current are simultaneously shown to show constant polarization saturation and the split component of polarization switching from each parent phase.

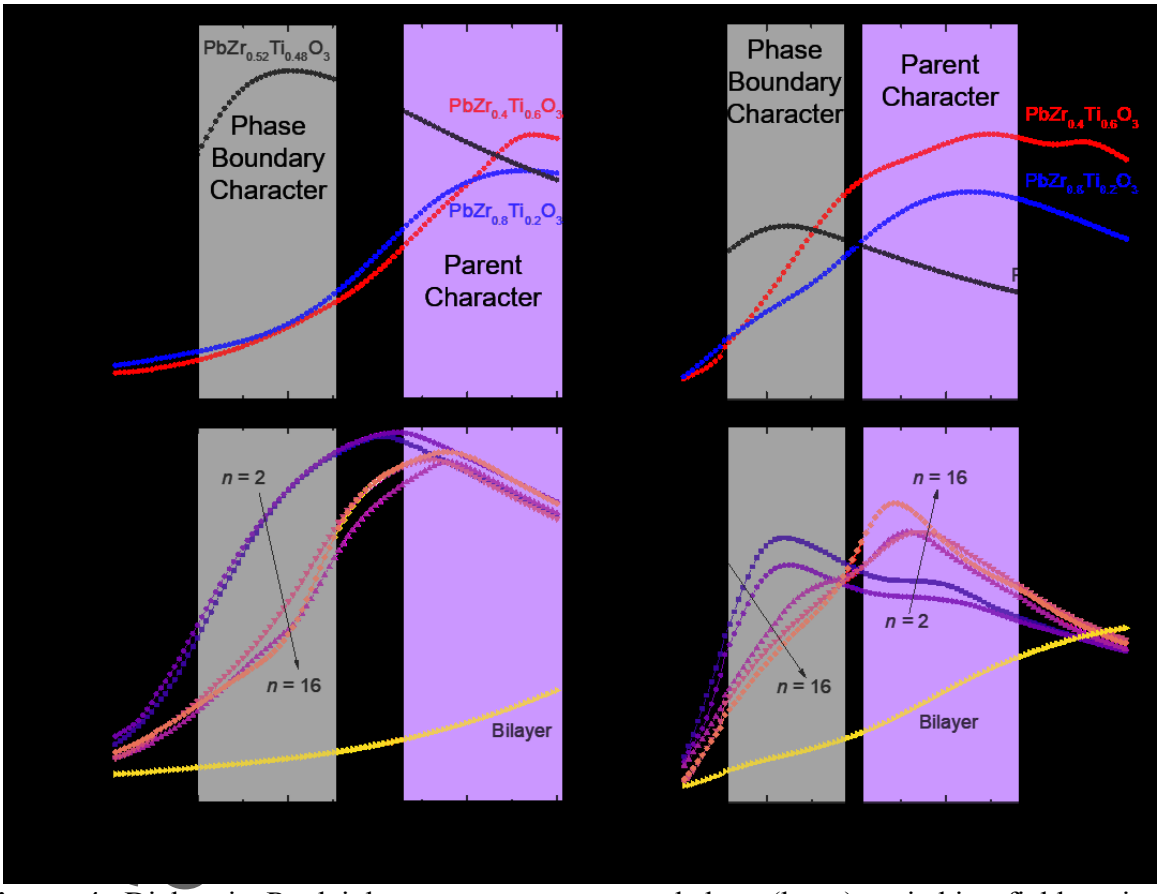

Figure 4. Dielectric Rayleigh measurements extended to (large) switching-field regimes indicating the response during switching (a) at large ac fields in the parent $PbZr_{0.8}Ti_{0.2}O_3$ and $PbZr_{0.4}Ti_{0.6}O_3$ phases and small ac fields in phase-boundary $PbZr_{0.52}Ti_{0.48}O_3$. (b) Similar data for the various superlattice samples exhibiting a mixture of both small- and large-field effects with $n = 2$, 4 superlattices showing predominant effects at lower fields and $n > 4$ superlattices predominant effects at higher fields. Corresponding dielectric loss for (c) the parent and phase-boundary materials indicating singular switching events which are contrasted with similar data for the (d) superlattice heterostructures which exhibit components of both parent and phase-boundary character.

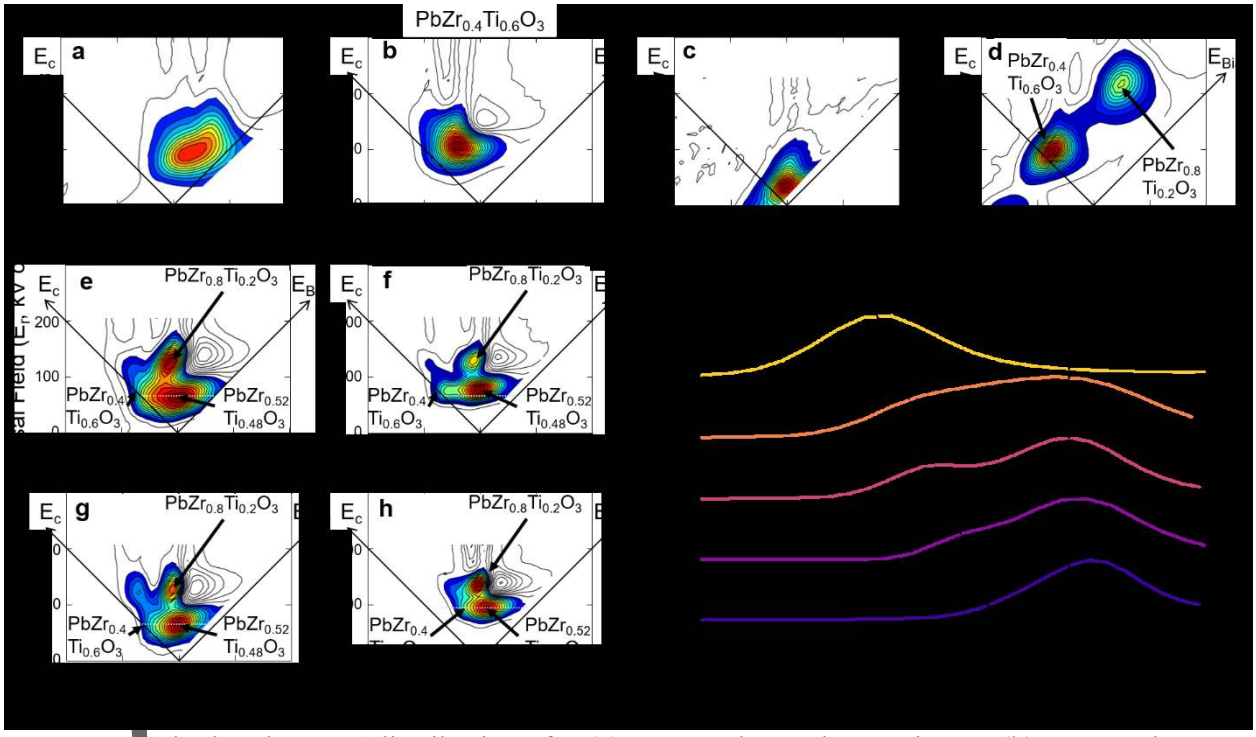

Figure 5. Calculated FORC distributions for (a) parent-phase $PbZr_{0.8}Ti_{0.2}O_3$, (b) parent-phase $PbZr_{0.4}Ti_{0.6}O_3$, (c) phase-boundary $PbZr_{0.52}Ti_{0.48}O_3$, (d) bilayer heterostructures as well as (e) n = 8, (f) n = 6, (g) n = 4, and (h) n = 2 superlattices. For each FORC analysis, distributions correspond to each of the parent phases and phase-boundary character are labeled/attributed. (i) A line profile taken across various contour plots in (d-h) at a reversal field of $E_r \approx 70$ kV cm^{-1} demonstrating the evolution of FORC distribution intensities with superlattice periodicity.

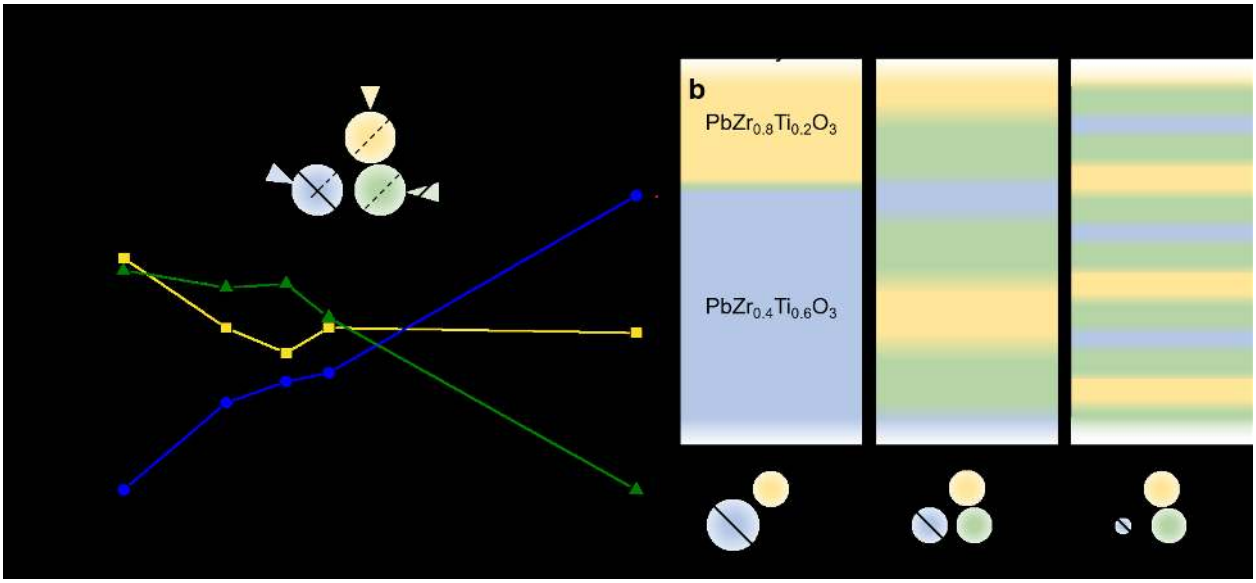

Figure 6. Additional analysis of the FORC data showing (a) the evolution of peak intensities for various FORC distributions as a function of superlattice periodicity. (b) Schematic representation of the evolution of peak intensities for various FORC distributions wherein an increasing phase-boundary-like green peak (quantitative based on the extracted to volume fraction) is found with decreasing superlattice periodicity (*n*).

Film	ε'_{ini}	α' (cm kV^{-1})	$\alpha'/\varepsilon'_{ini}$ (cm kV^{-1})
$PbZr_{0.8}Ti_{0.2}O_3$	362	2.8	0.008
$PbZr_{0.4}Ti_{0.6}O_3$	338	4.1	0.012
$PbZr_{0.52}Ti_{0.48}O_3$	865	87.6	0.101
Bilayer	370	2.8	0.007
n = 16	613	16.8	0.027
8	583	16.8	0.029
6	567	16.6	0.029
4	805	32	0.040
2	515	13.5	0.026

Table 1. Dielectric Rayleigh parameters of various superlattice films and heterostructures.

Simultaneous large susceptibility and polarization in the $PbZr_{1-x}Ti_xO_3$ system is observed as a function of superlattice periodicity utilizing unit-cell precise pulsed-laser deposition. $(PbZr_{0.8}Ti_{0.2}O_3)_n/(PbZr_{0.4}Ti_{0.6}O_3)_{2n}$ superlattices exhibit a large volume fraction of morphotropic phase-boundary-like character at the interfaces, which enables large permittivity while remnant parent phases maintain large polarization.

Keyword ferroelectricity

Eduardo Lupi, Anirban Ghosh, Sahar Saremi, Shang-Lin Hsu, Shishir Pandya, Gabriel Velarde, Abel Fernandez, R. Ramesh, Lane W. Martin*

Large Polarization and Susceptibilities in Artificial Morphotropic Phase Boundary $PbZr_{1-x}Ti_xO_3$ Superlattices

ToC figure

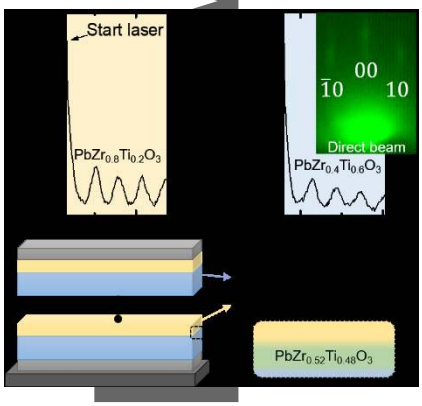

Supporting Information

Large Polarization and Susceptibilities in Artificial Morphotropic Phase Boundary $PbZr_{1-x}Ti_xO_3$ Superlattices

*Eduardo Lupi, Anirban Ghosh, Sahar Saremi, Shang-Lin Hsu, Shishir Pandya, Gabriel Velarde, Abel Fernandez, R. Ramesh, Lane W. Martin**

I. Superlattice Composition Series

A series of $(PbZr_{0.8}Ti_{0.2}O_3)_n/(PbZr_{0.4}Ti_{0.6}O_3)_m$ superlattices with varying average composition was grown using the same procedure outlined in the main text (Experimental Section). The ratio $n \times m$ was adjusted to 7 × 5, 5 × 7, 4 × 8, and 3 × 9 corresponding to average superlattice compositions of $PbZr_{0.63}Ti_{0.37}O_3$, $PbZr_{0.57}Ti_{0.43}O_3$, $PbZr_{0.53}Ti_{0.47}O_3$, and $PbZr_{0.5}Ti_{0.5}O_3$, respectively. θ-2θ X-ray scans show high-quality epitaxial superlattices (**Figure S1**a). The $SL_{(0)}$ 002 peak shifts to a smaller out-of-plane lattice parameter at the near-phase-boundary composition (47% $PbTiO_3$), consistent with expectations for this material system and the observed dielectric permittivity (Figure S1b). The evolution of dielectric permittivity across a range of frequencies (1-100 kHz) confirms phase-boundary-like behavior at an average composition of $PbZr_{0.53}Ti_{0.47}O_3$ (*i.e.*, the 4 × 8 superlattice).

II. X-ray Diffraction Studies

Full-range θ-2θ X-ray diffraction patterns about the 001- and 002-diffraction conditions for superlattices of various periodicities and accompanying reference films demonstrate excellent epitaxial crystalline quality (**Figure S2**). Single peaks in the 002-condition can be seen for all

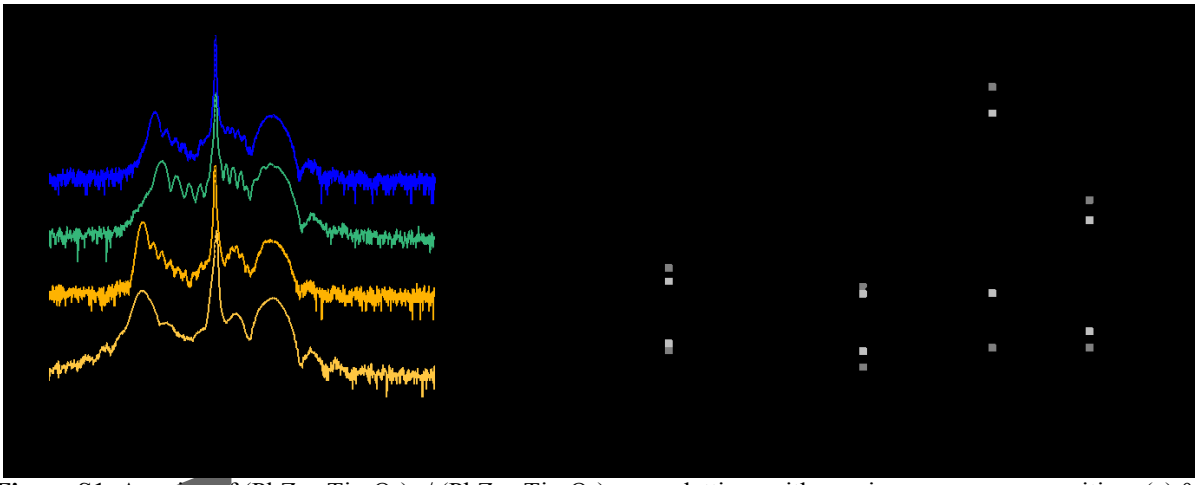

Figure S1. A series of $(PbZr_{0.8}Ti_{0.2}O_3)_n$ / $(PbZr_{0.4}Ti_{0.6}O_3)_m$ superlattices with varying average composition. (a) θ-2θ X-ray scans and (b) dielectric permittivity reveal phase boundary-like behavior at an average mole fraction of $PbTiO_3$ of 47%, as in $PbZr_{0.53}Ti_{0.47}O_3$.

films except for the bilayer heterostructure, wherein two peaks are seen (as expected), one for each of the parent phase constituents.

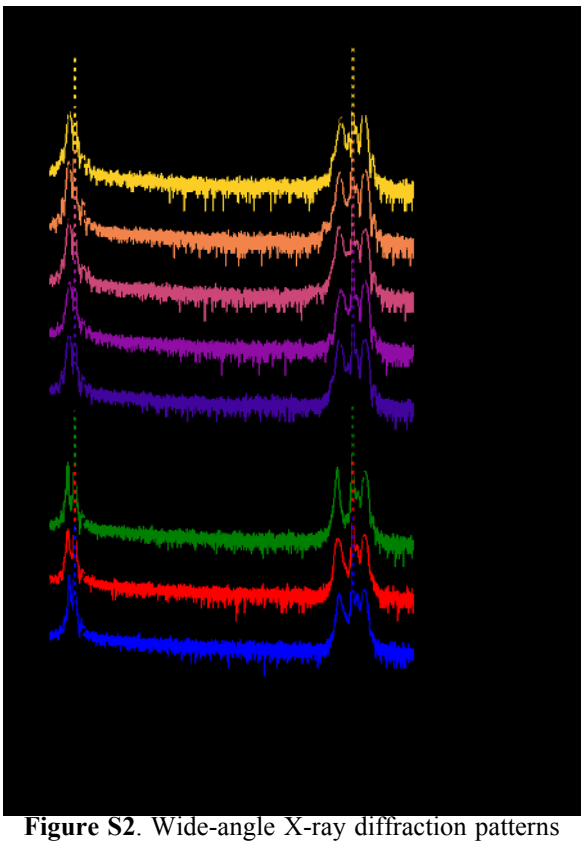

Figure S2. Wide-angle X-ray diffraction patterns about the 001- and 002- diffraction conditions.

III. Reciprocal Space Maps

Reciprocal space mapping studies about the 103_{pc}-diffraction condition indicate partial relaxation of the $PbZr_{0.8}Ti_{0.2}O_3$ film due to its large (-2.5%) compressive strain imposed by the $PrScO_3$ substrate (**Figure S3**a). The $PbZr_{0.4}Ti_{0.6}O_3$ parent film and the $PbZr_{0.52}Ti_{0.48}O_3$ film demonstrate fully-strained epitaxy (Figure S3b-c), consistent with all superlattices (Figure S3d-h) on the same substrate. The bilayer film also has some partial relaxation due to it having a thick layer (27 nm) of $PbZr_{0.8}Ti_{0.2}O_3$ (Figure S3i).

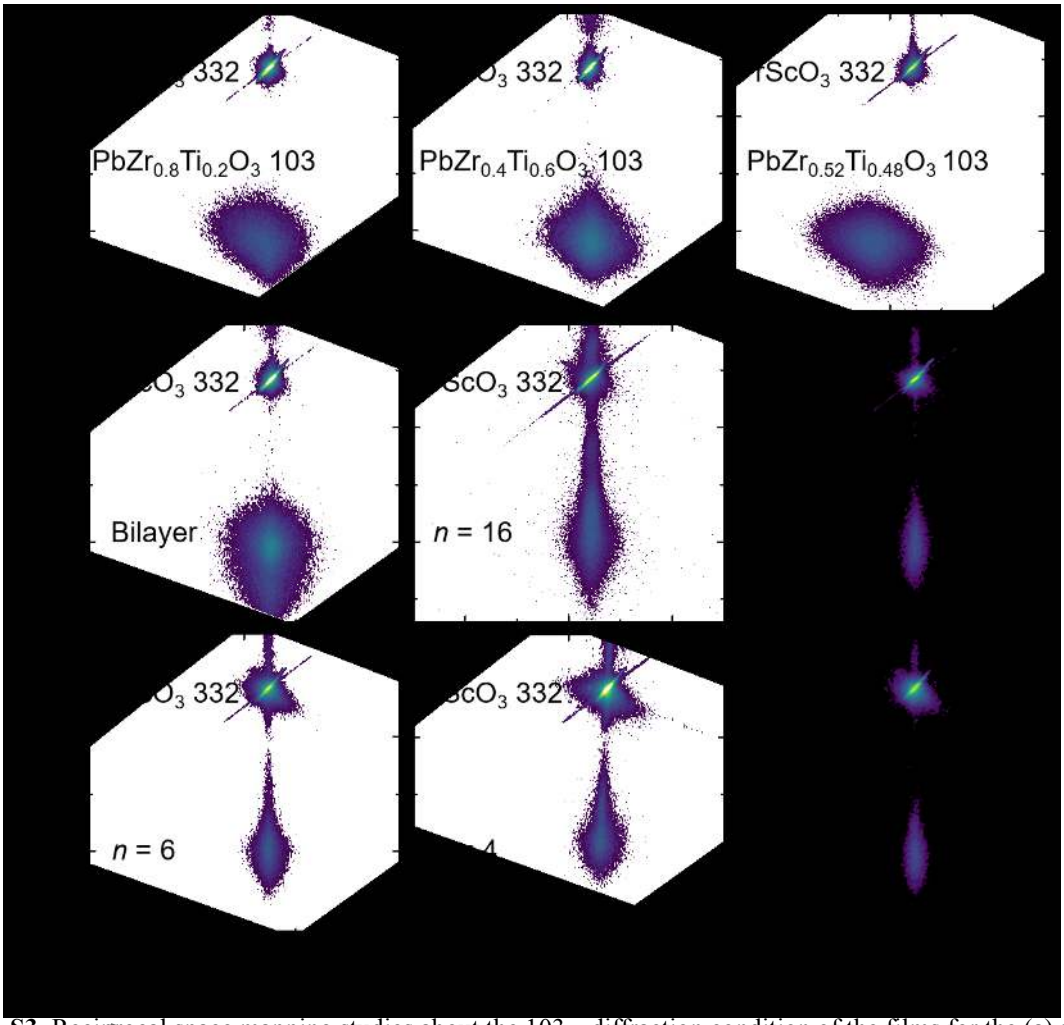

Figure S3. Reciprocal space mapping studies about the 103_{pc}-diffraction condition of the films for the (a) parent-phase $PbZr_{0.8}Ti_{0.2}O_3$, (b) parent-phase $Pb_{0.4}Ti_{0.6}O_3$, (c) phase-boundary $PbZr_{0.52}Ti_{0.48}O_3$, (d) bilayer heterostructure as well as the (e) n = 16, (f) n = 8, (g) n = 6, (h) n = 4, and (i) n = 2 superlattices. All heterostructures and superlattices grown demonstrate excellent crystalline quality.

IV. Scanning Transmission Electron Microscopy Studies

Z-contrast, high-angle annular dark-field (HAADF) scanning transmission electron microscopy (STEM) imaging of two superlattice structures – namely the $(PbZr_{0.8}Ti_{0.2}O_3)_n/(PbZr_{0.4}Ti_{0.6}O_3)_{2n}$ with n = 6, 8 hetersotructures were completed and confirm the production of high-quality structures. A lower-resolution image across a wide area of the heterostructure, here for a n = 8 superlattice, reveals smooth interfaces with no apparent defect structures (**Figure S4**a). Additional atomic-resolution imaging, here at the interface between the bottom electrode and superlattice structure, further confirms the high-quality structures and highly commensurate nature of the interface (Figure S4b). As noted in the main text, due to the presence of the same cations (*i.e.*, lead, zirconium, and titanium) in both

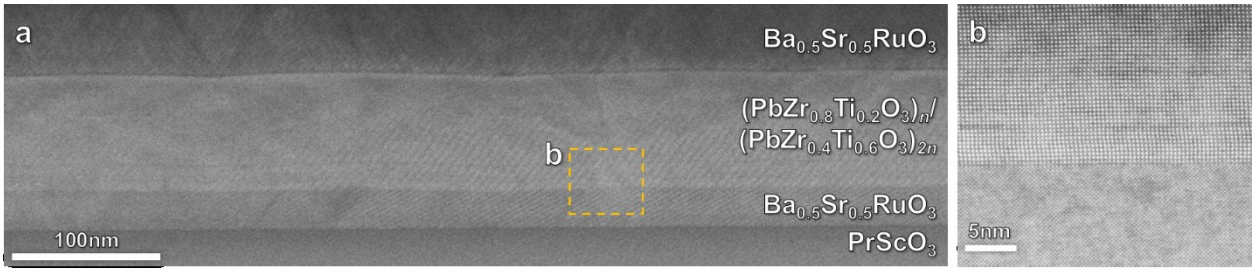

Figure S4. Scanning Transmission Electron Microscopy (STEM) imaging of superlattice structures reveals high quality epitaxial growth, on (a) full heterostructure and (b) atomically-precise scales.

layers of the superlattice, the z-constrat is rather weak, but the structure found to be high quality nonetheless.

V. Transition Temperatures

The ferroelectric Curie temperature was confirmed to be 500, 580, and 560°C for $PbZr_{0.8}Ti_{0.2}O_3$, $PbZr_{0.4}Ti_{0.6}O_3$, and n = 4 superlattices, respectively (**Figure S5**). Intermediate-period (n = 4) superlattices were measured as this sample had the largest enhancement of

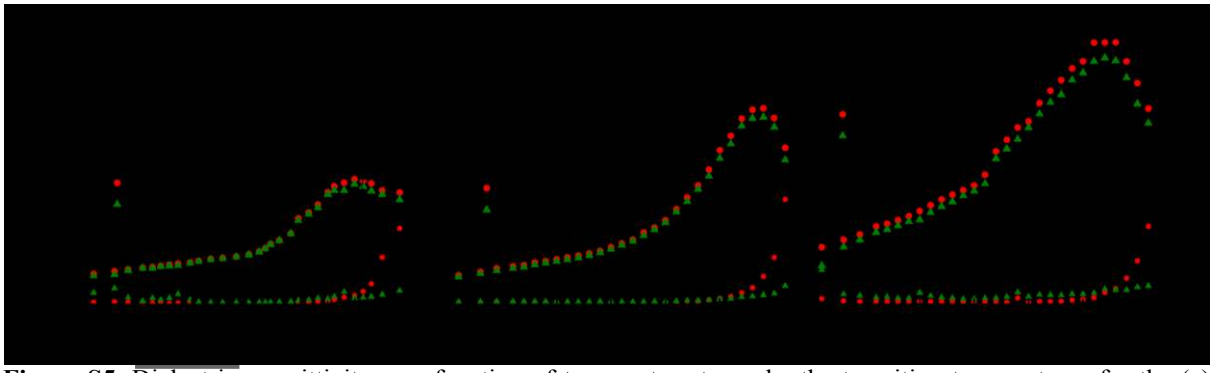

Figure S5. Dielectric permittivity as a function of temperature to probe the transition temperatures for the (a) parent-phase $PbZr_{0.8}Ti_{0.2}O_3$, (b) parent-phase $PbZr_{0.4}Ti_{0.6}O_3$, and (c) $n = 4$ superlattices.

dielectric permittivity at room temperature. This consistency rules out a diminished transition temperature as the cause of dielectric enhancement.

VI. Rayleigh Dielectric Measurements – Reference Films

Rayleigh dielectric (ac-field dependent) measurements were performed on the parent phases, bilayer heterostructures, and phase-boundary films in addition to all superlattices (**Figure S6**). The phase-boundary $PbZr_{0.52}Ti_{0.48}O_3$ exhibits both the largest slope and y-intercept, interpreted as Rayleigh parameters α' and ε'_{ini}, respectively. Enhanced values for these parameters indicate phase-boundary behavior for the $PbZr_{0.52}Ti_{0.48}O_3$ composition and parent-like behavior for bilayer heterostructures (Table 1).

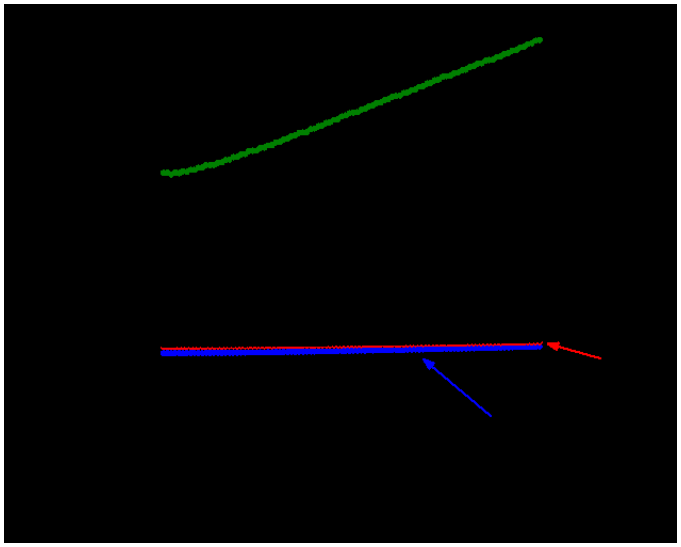

Figure S6. Rayleigh dielectric measurements on reference samples (parent phases, bilayer heterostructures, and phase-boundary films) taken at 1 kHz.

Figure S7. Minor ferroelectric hysteresis polarization – electric field loops taken at 1 kHz from which FORC plots are extracted.

VII. Ferroelectric Hysteresis Minor Loops

First-order reversal curve (FORC) analysis was accomplished by taking multiple minor ferroelectric hysteresis loops. Parent-phase $PbZr_{0.8}Ti_{0.2}O_3$ shows two switching steps, consistent with the partial relaxation of this thick (80 nm) layer (**Figure S7**a). Parent-phase $PbZr_{0.4}Ti_{0.6}O_3$ demonstrates a singular switching event and a large saturation polarization, whereas phase-boundary $PbZr_{0.52}Ti_{0.48}O_3$ has a much smaller saturation polarization and coercive field (Figure S7b-c). Bilayer heterostructures have three distinct switching regimes attributed to the convolution of both strained parent phases and the partially relaxed $PbZr_{0.8}Ti_{0.2}O_3$ (Figure S7d). Superlattice films demonstrate similar saturation polarization to that of the parent phases, yet have more subtle behavior revealed by FORC analysis (Figure S7e-h).